Sensing free surface of arc weld pool using specular reflection: principle and analysis

R Kovacevic, PhD, MemASME, SMSME, MAWS and **Y M Zhang,** PhD, MemASME, SMSME, MAWS, MIEEE
Center for Robotics and Manufacturing Systems, University of Kentucky, Lexington, Kentucky, USA

The weld pool surface provides important information for understanding arc welding processes. In this study, a novel vision sensor is proposed to measure the three-dimensional shape of the free weld pool surface. A pulsed laser is projected on to the weld pool through a specific grid. Specular reflection from the pool surface is sensed using a high shutter speed camera. The three-dimensional weld pool surface shape is clearly shown by the specular reflection. To determine the shape of the pool surface, an image processing technology has been developed to extract the skeleton of the specular reflection from the acquired image. The imaging principle is analysed to determine the correlation between the reflection and the weld pool surface. If the weld pool surface is known, the corresponding specular reflection can be directly calculated using the imaging model which is derived based on the reflection law. However, no explicit models can be obtained to determine the weld pool surface using the reflection and sensor parameters. To solve this difficulty, an iterative algorithm is proposed. The weld pool surface can now be calculated in 1 second from the specular reflection of the weld pool surface. A higher calculation speed is currently being pursued.

Key words: weld pool, pool surface, pool depression, GTAW, machine vision

NOTATION

d	distance from the pinhole to the image coordinate origin
I_k	number of discrete points on stripe skeleton k
$oxyz$	reference coordinate system
$o_i x_i y_i$	image coordinate system
(x_{g0}, x_{g1})	end-point coordinates of the slits (along the x direction)
$(x_i(i), y_i(i))$ $(1 \leqslant i \leqslant I_k)$	coordinate of the ith discrete point on stripe skeleton k in the image coordinate system
(x_p, y_p, z_p)	coordinate of the pinhole in the reference coordinate system
(x_s, y_s, z_s)	weld pool surface point, described using the reference coordinate
$(x_s(i), y_s(i), z_s(i))$	point of the weld pool surface corresponding to $(x_i(i), y_i(i))$
$y_i = s_k(x_i)$	skeleton equation of the kth laser stripe in the image coordinate system, corresponding to slit k
(y_k, z_k)	coordinate of the central line of the kth slit in the yz plane $(1 \leqslant k \leqslant K)$
(y_{k0}, y_{k1})	range of the kth slit: $y_{k0} < y_{k1} < y_{(k+1)0} < y_{(k+1)1}$ $(1 \leqslant k \leqslant K-1)$
z'_{x_s}, z'_{y_s}	slopes of the weld pool surface at (x_s, y_s) along the x and y directions respectively
γ	$\gamma = y_k - y_p$
ρ_g, z_g	placement parameters of the grid in the yz plane
ρ_{ix}, ρ_{iy}	slopes of the incident ray along the x and y directions respectively
ρ_{nx}, ρ_{ny}	slopes of the normal along the x and y directions respectively
ρ_{px}, ρ_{py}	slopes of the reflected ray along the x and y directions

The MS was received on 10 May 1995 and was accepted for publication on 22 March 1996.

1 INTRODUCTION

Strictly speaking, no flat weld pool surfaces exist in arc welding processes. Pool surface deformation can always be observed in gas metal arc welding (GMAW) and gas tungsten arc welding (GTAW) with filler, due to the mass transfer. For GTAW without filler, pool surface deformation is apparent in the full penetration mode. In the case of partial penetration, three modes of pool deformation can be observed for different current levels (**1**). Thus, the deformation of the pool surface is an inherent characteristic of arc welding processes. The observation of the weld pool surface is, therefore, essential and necessary for studying arc welding processes. Furthermore, surface deformation is an important phenomenon in the arc welding process because of its influence on the arc energy distribution (**1, 2**), its correlation with possible weld defects (**2**), and correlation to the weld penetration (**1, 3**). To study the pool behaviour more realistically, free pool surfaces have been incorporated and several numerical models have been proposed (**4–8**). Since the validity of the developed models should be judged based on practical measurements, pool surface measurement also plays an important role in numerical model development, which is recognized as the only way to acquire a thorough understanding of the physical processes occurring in the weld pool.

A possible application of pool surface shape sensing is the monitoring and control of weld quality, specifically of weld penetration. It is known that weld penetration control is a crucial research subject in automated welding. The difficulty associated with this problem is to find a precise and reliable way to measure the weld penetration using only top-side sensors which are attached to and move with the torch. Among the

methods proposed in existing literature, pool oscillation (**9–15**) and infra-red sensing (**16–20**) based methods received more attention. [Ultrasonic sensing (**21–25**) and radiographic sensing (**1, 26, 27**) use additional sensing devices which are difficult to attach to the torch.] Acoustic emission sensing (**28**) can distinguish between full penetration and partial penetration. Though many methods are available to measure the weld penetration, in order to improve the quality of welding, new or improved solutions are still strongly needed because of the inherent restrictions associated with each of the above-mentioned methods. It was reported in a previous study (**29**) that a skilled human welder can extract penetration information by viewing the weld pool. Due to the difficulty involved in real-time pool surface shape measurement, the geometry of the sag behind the pool was measured as an alternative (**30**). It was found that the average weld depression depth h, which is defined as the cross-weld depression area divided by the weld width, has a close relationship with the full penetration state which is specified by the back-side bead width (**29**). Based on the dynamic analysis and modelling (**31**), a corresponding closed-loop control system has been developed, and satisfactory control has been obtained (**30**). However, there is an inherent measurement delay if the weld behind the pool is monitored rather than the pool itself. If the pool surface shape can be measured, a promising weld penetration control can be expected.

Although the surface shape measurement of the arc weld pool is important, a literature survey shows that limited work has been done in this area due to the extreme difficulty associated with this problem. The pioneering work was conducted at the Ohio State University by Rokhlin and Guu (**1, 26, 27**), using radiography. The radiation of the received X-ray increases with the depression depth. Using this approach, many valuable results have been acquired based on pool surface measurements (**1, 26, 27**). However, only the case of stationary arc was addressed. To avoid the interference of the electrode and gas nozzle, long electrode extension and inclined torch attitude were used. The imaging device and X-ray source could not both be attached to the torch to form a so-called top-side sensor. This fact, in addition to the radioactivity, restricts the prospective application of this method in practical monitoring or control of weld pools. Also, the principle behind this method is to measure the material thickness. For the case of full penetration where the back-side pool surface deformation occurs, the pool surface shape will be difficult to extract.

A novel mechanism for observing the pool surface shape is proposed in this paper. Structured-light stripes generated by projecting a laser through a novel grid are reflected from the mirror-like pool surface (**32**). The deformation of the stripes is determined by the deformation of the weld pool surface. Thus, the sensed reflection of the stripes can be processed and used to compute the three-dimensional pool surface. The entire sensor is attached to and moves with the torch. It will be shown that the correlation between the weld pool surface and the resultant image is governed by the reflection law, despite the penetration mode. Hence, both the partial penetration and full penetration weld pool surfaces can be measured if the weld pool is not depressed to the extent that the incident or reflected laser rays are interrupted.

2 SENSING PRINCIPLE AND SET-UP

2.1 Principle

The proposed sensing system is shown in Fig. 1. To sense the three-dimensional shape of a weld pool surface, the influence of the arc light must first be eliminated. A short-duration pulsed laser is projected on to the weld pool. The camera shutter is synchronized with the pulse duration. During the laser pulse, the laser intensity is much stronger than the arc intensity. Thus, if the shutter speed is fast enough, the arc light can be essentially eliminated from the image (**33**).

To acquire the three-dimensional weld pool surface information, a special technique must be implemented. The common practice for determining the three-dimensional shape of a surface is to project a structured light on to the surface and sense the diffuse reflection of the structured light (**34–36**). The shape information can then be extracted from the deformation of the structured light. However, the weld pool surface is mirror-like smooth and no substantial amount of structured light can be reflected diffusely. It appears that only specular reflection can be utilized.

In the case of specular reflection, the observed scene is the virtual image of the original object (**37**). The relationship between the original and its virtual image is determined by the shape of the mirror surface. Usually, structured light is formed by projecting a laser through a grid. The sole function of the grid is to form the structured light stripes. As the light passes through the grid, its direction of travel is unchanged. This causes the virtual image of a laser point source to be a single spot despite the shape of the mirror-like surface (see Fig. 2a). Thus, a bright spot is sensed by the camera (see Fig. 2b), and no shape information of the reflection surface is contained in the image. To acquire the shape information, a novel incident mechanism of structured light, (as shown in Fig. 3) is proposed.

The proposed incident mechanism of structured light is realized through a specialized grid. This grid consists of a common grid and frosted glass. When the laser is projected on to the frosted glass, the laser travel direction will be changed (see Fig. 3). From the viewpoint of light travel, any point on the frosted glass can be considered as a new point light source which disperses light with a certain diffuse angle (see Fig. 3). The camera views the slits (grid openings) through their reflection from the weld pool surface. Their virtual image consists of bright stripes deformed by the weld pool surface deformation (Fig. 3) and is sensed by the camera. The resultant images are shown in Fig. 4. The surface shape of the weld pool is contained in the acquired image.

2.2 Set-up

A vision system with pulsed laser illumination is used to perform the sensing of the weld pool surface. This system has been used to sense the two-dimensional boundary of the weld pool in previous work (**33, 38**). It consists of a strobe illumination unit (pulsed laser), camera head and system controller (**39**). The pulse of

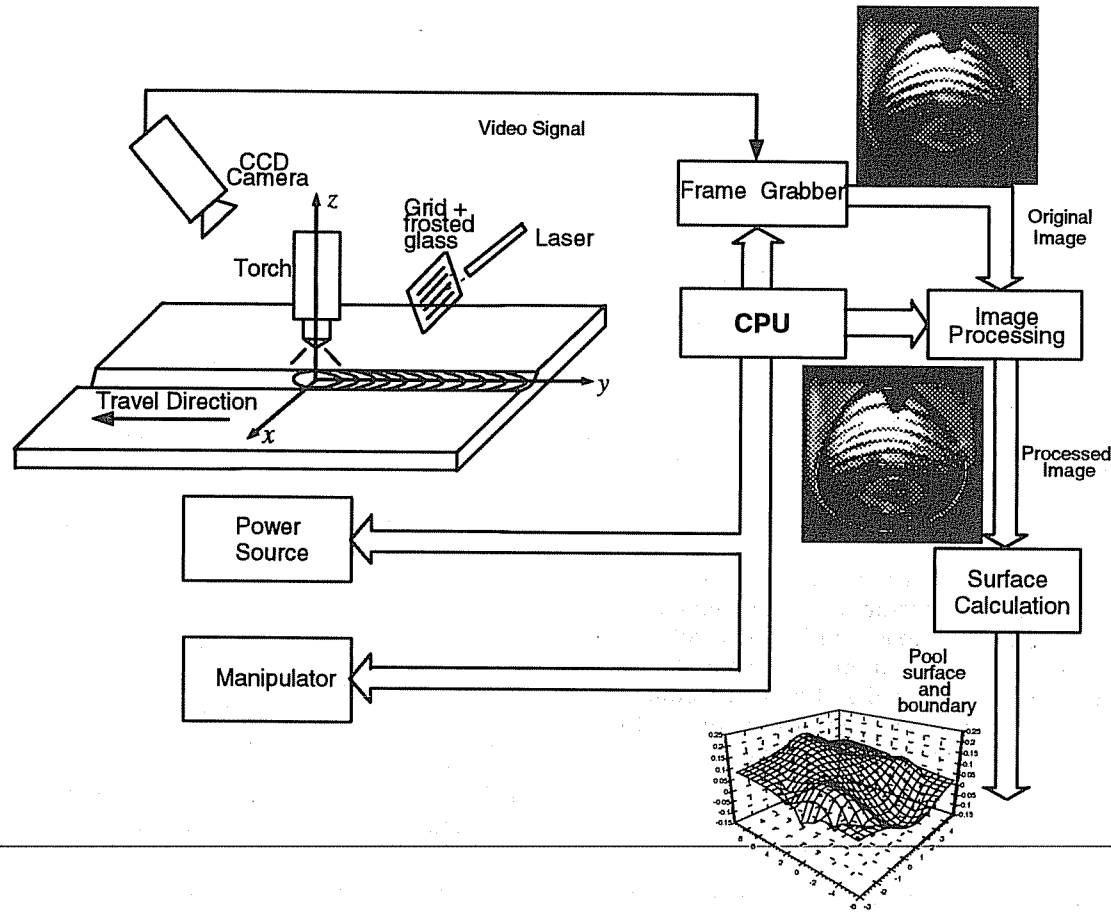

Fig. 1 Sensing system of weld pool surface shape

the laser illumination lasts only 3 ns. Although the average power of the laser is only 7 mW, its pulse power reaches 50 kW. During the pulse, the camera shutter is opened to capture the scene. To further improve the signal–noise ratio, a narrow-band optical filter has been used to match the laser wavelength (337 nm). Thus, a clear reflection of the projected laser can be acquired. The video signal from the camera is digitized into 512 × 512 digital matrices by a frame grabber.

Beads on plate welds were made of 3 mm stainless steel 304 using the DCEN gas tungsten arc welding. The experimental set-up is shown in Fig. 1. The welding current is controlled by a computer through its analogue output to the power supply, ranging from 10 to

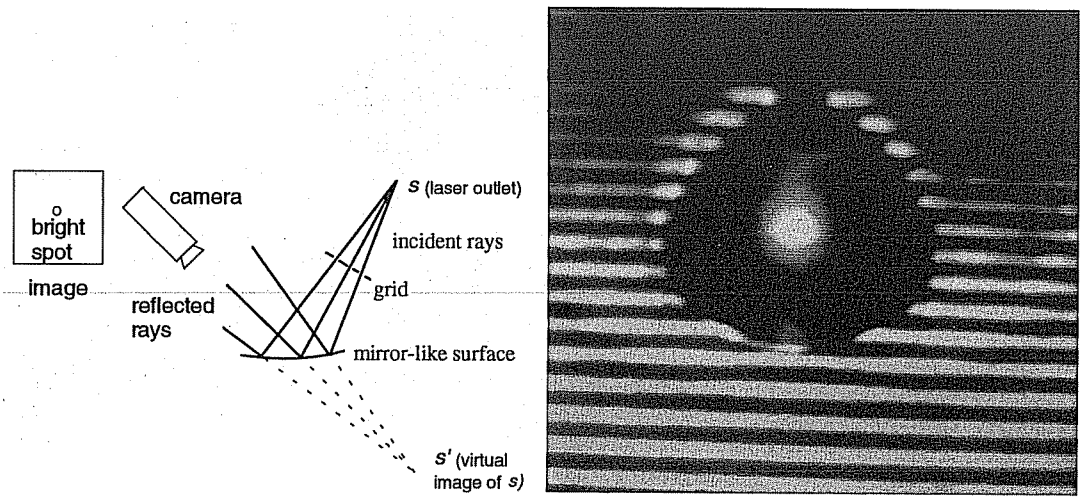

Fig. 2 Specular reflection of the weld pool with conventional sensor: (a) optical principle and (b) image. The virtual image is a spot in this case. The sensed specular reflection is a bright spot as shown in (b) and contains no information about the weld pool surface

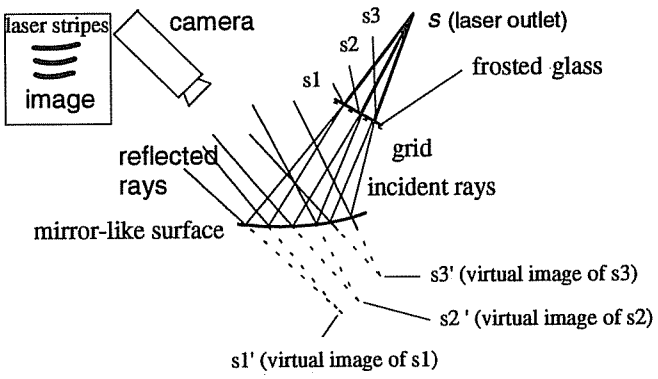

Fig. 3 Proposed sensing principle for specular reflection. The laser stripes can be sensed by the camera as shown in Fig. 4. The deformation of the laser stripes reflects the shape of the weld pool surface

200 A. The torch and camera are attached to a three-axis manipulator. The motion of the manipulator is controlled by the three-axis motion control board which receives commands from the computer. The motion can be preprogrammed and on-line modified by the computer in order to achieve the required torch speed and trajectory, including the arc length.

3 IMAGING MODEL

The proposed sensing principle can be exactly described by a mathematical model. It will be shown that, for any given weld pool surface, the corresponding image can be calculated using the mathematical model and sensor parameters.

Establish the reference coordinate system $oxyz$, as shown in Fig. 1, where the xy plane is parallel with the ground surface (that is the z axis is vertical). The torch travels along the negative y axis. The workpiece surface lies approximately on the xy plane.

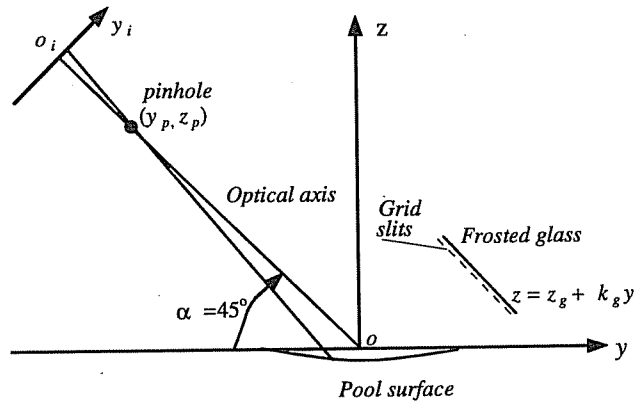

Fig. 5 The yz plane view

The weld pool surface can be denoted by the following equation:

$$z = f(x, y) \tag{1}$$

Adjust the optical axis of the camera to lie on the yz plane and pass through the origin o with an angle $\alpha = 45°$ (see Fig. 5). Establish the image plane coordinate system $o_i x_i y_i$ where the x_i axis is along the horizontal scan direction of the camera (see Fig. 6). The origin o_i is the point intersected by the optical axis and the image plane (Fig. 6). Denote the coordinate of the pinhole (**40**) in the reference coordinate system as (x_p, y_p, z_p). It is known that $x_p = 0$. The slits of the grid from which the structured light disperses are described by the following equations:

$$\begin{aligned} &z = z_g + \rho_g y \qquad (y_{k0} \leqslant y \leqslant y_{k1},\ 1 \leqslant k \leqslant K) \\ &x_{g0} \leqslant x \leqslant x_{g1} \end{aligned} \tag{2}$$

where $z_g$and ρ_g are the placement parameters of the grid plate (see Fig. 5), y_{k0} and y_{k1} $(y_{k0} < y_{k1})$ are the parameters of the kth slit and K is the number of slits in the grid.

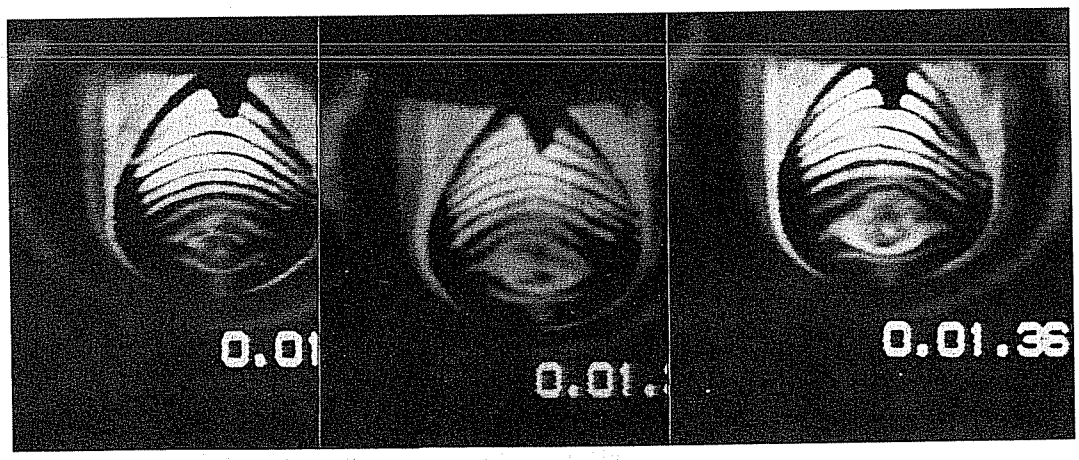

(a) (b) (c)

Fig. 4 Images acquired by the proposed sensor: (a) current = 112 A, partial penetration; (b) current = 118 A, full penetration, back-side bead width 2.6 mm; (c) current 119 A, full penetration, back-side bead width 2.7 mm. GTA welding without filler, torch speed 2 mm/s, arc length 3.0 mm, 3 mm stainless steel, argon flowrate 7 l/min, back-side argon flowrate 2 l/min

The laser passing through the slits travels with a diffusion angle, and a region on the workpiece surface will be illuminated by this laser. Consider a point (x_s, y_s, z_s) on the weld pool surface (Fig. 6). For the reflected rays from this point, only the ray that crosses the pinhole will be sensed by the camera (Fig. 6). The equation of this reflected ray is

$$\frac{x - x_s}{x_p - x_s} = \frac{y - y_s}{y_p - y_s} = \frac{z - z_s}{z_p - z_s} \tag{3}$$

To generate this reflected ray, there must be a corresponding incident ray. It is known that the normal of the surface at this point is

$$\frac{x - x_s}{z'_{x_s}} = \frac{y - y_s}{z'_{y_s}} = -(z - z_s) \tag{4}$$

where

$$z'_{x_s} = \left.\frac{\partial z}{\partial x}\right|_{x=x_s,\, y=y_s} \quad \text{and} \quad z'_{y_s} = \left.\frac{\partial z}{\partial y}\right|_{x=x_s,\, y=y_s}$$

According to the reflection law, the incident ray that can produce the reflected ray (3) can be determined through the normal (4) and the reflected ray (3). Thus, the following equation can be acquired to describe the qualified incident ray:

$$\rho_{ix}(x - x_s) = \rho_{iy}(y - y_s) = z - z_s \tag{5}$$

where ρ_{ix} and ρ_{iy} are constants which are given in the following equations:

$$\frac{\rho_{rx} - \rho_{nx}}{1 + \rho_{rx}\rho_{nx}} = \frac{\rho_{nx} - \rho_{ix}}{1 + \rho_{nx}\rho_{ix}}$$
$$\frac{\rho_{ry} - \rho_{ny}}{1 + \rho_{ry}\rho_{ny}} = \frac{\rho_{ny} - \rho_{iy}}{1 + \rho_{ny}\rho_{iy}} \tag{6}$$

where ρ_{rx} and ρ_{ry} are the x and y directional slopes of the reflected ray and ρ_{nx} and ρ_{ny} are the x and y directional slopes of the normal:

$$\rho_{rx} = \frac{z_s - z_p}{x_s - x_p}$$
$$\rho_{ry} = \frac{z_s - z_p}{y_s - y_p}$$
$$\rho_{nx} = \frac{-1}{z'_{x_s}} \tag{7}$$
$$\rho_{ny} = \frac{-1}{z'_{y_s}}$$

Thus, for any given weld pool surface $z = f(x, y)$, the resultant image can be computed using the aforementioned mathematical description of the sensing process.

Assume that the pool boundary curve is $y = b_0(x)$ (see Fig. 6). The given sensor configuration can be described by (x_p, y_p, z_p) and equations (2). The corresponding image is unique and can be determined by the following procedure:

1. For possible (x, y) (see Fig. 6), if it is surrounded by the pool boundary $y = b_0(x)$ on the xy plane, select it as (x_s, y_s) and calculate z_s using equation (1). Thus, (x_s, y_s, z_s) is a point on the weld pool.
2. For (x_s, y_s, z_s), calculate ρ_{ix} and ρ_{iy} for the incident ray which makes the reflected ray cross the pinhole of the camera using equations (6) and (7).
3. Calculate the intersection between line (5) and the grid plane. If the intersection falls on the slits described in (2), a qualified ray is found and the corresponding imaging will be the intersection between its reflected ray (3) and the image plane. Otherwise, no corresponding imaging exists for the point (x_s, y_s, z_s).

4 OBSERVATION AND ANALYSIS

4.1 Reflection

When a fixed flat mirror is used as the specular surface, straight stripes are observed despite different slopes. The distance, that is the stripe distance between two adjacent stripes, is equal. (The slits of the grid are equally spaced.) However, the stripe distance depends

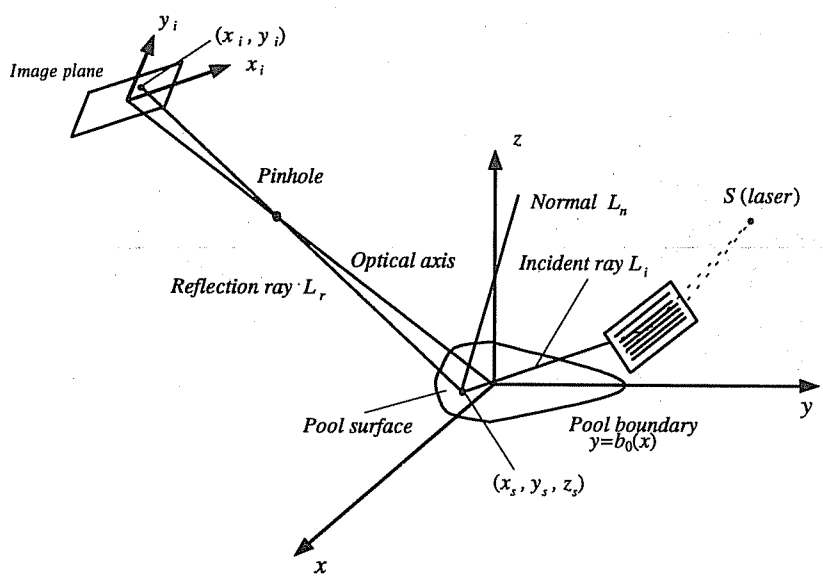

Fig. 6 Reflection principle

on the placement slope, z'_{y_s}, of the mirror. The stripe distance decreases roughly linearly with the slope.

Observe the image in Fig. 4b. Generally speaking, the stripe distance increases towards the rear of the weld pool from the depressed area. Thus, the slope therefore decreases towards the rear of the weld pool. Assume d_0 is the stripe distance when $z'_{y_s} = 0$. From the depressed area towards the rear, the surface height increases before the stripe distance reaches d_0. Then the surface height decreases.

The weld pool can be approximately classified into the impacted and non-impacted zones (Fig. 7). It can be seen that the stripes at the non-impacted zone are similar. However, the reflection at the impacted zone is more complicated. Both concave and convex stripes are observed. It can also be observed that the convex stripe may develop into a closed contour (Fig. 4b and c) from the single stripe (Fig. 4a). Thus, two different modes of the reflection can be encountered at the impacted zone, that is open-contour and closed-contour modes (Fig. 8). It is also observed that the closed-contour mode occurs when increasing the depression. The depression degree is directly related to the shape of the closed contour. When the closed contour is enlarged, the depression increases (Fig. 4b and c).

In the non-impacted zone, the stripes are very pronounced. However, in the impacted zone, such a pure stripe mode is not well maintained. Although the stripes can still be identified from the impacted zone, bright regions also exist between the stripes and inside the closed contour. If the depressed area is perfectly smooth, no such phenomenon should be observed. However, because of possible surface impurities, electrode tip irregularity, etc., the distribution of the impact of the plasma jet on the weld pool may not be perfectly smooth. Also, the high-frequency components of the pool oscillation may influence the distribution of the plasma jet field. The non-uniform plasma jet distribution field and oscillated pool surface can be coupled. No stationary and smooth plasma jet distribution can be expected. As a result, the depressed surface may not be perfectly smooth. The local surface slope can severely change within a small region. Thus, the reflection may no longer exhibit the pure stripe mode as it does in the non-impacted zone (Fig. 4b).

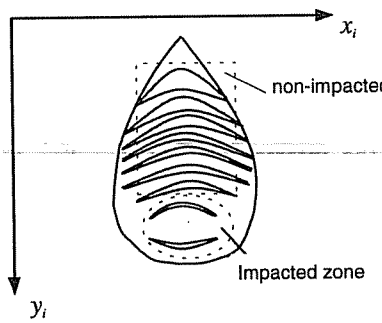

Fig. 7 Weld pool zones

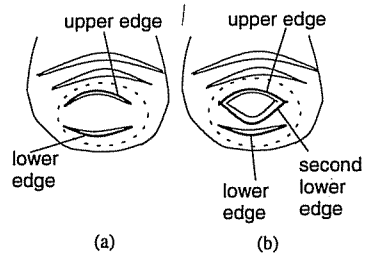

Fig. 8 Reflection modes at impacted zone: (a) open-contour mode, (b) closed-contour mode

4.2 Individual stripe

Assume $y_i = s_k(x_i)$ is the skeleton of the kth laser stripe (Fig. 9). Denote the intersected points, that is the beginning and ending point of the kth reflection skeleton, between the pool boundary and the skeleton $y_i = s_k(x_i)$ as $(x_i(1), y_i(1))$ and $(x_i(I_k), y_i(I_k))$. Denote $(x_i(i), y_i(i))$ $(1 \leqslant i \leqslant I_k)$ as the ith point of the skeleton. (The skeleton is a set of discrete points on the image plane.) Assume that $(x_s(1), y_s(1), z_s(1))$ and $(x_s(i), y_s(i), z_s(i))$ are the points on the weld pool surface corresponding to $(x_i(1), y_i(1))$ and $(x_i(i), y_i(i))$ respectively. Their projections on to the yz plane are $(x_s(1), y_s(1))$ and $(x_s(i), y_s(i))$ respectively. Also, the projections of $(x_i(1), y_i(1))$ and $(x_i(i), y_i(i))$ on to the y_i axis are $y_i(1)$ and $y_i(i)$.

In order to show that $-[y_i(i) - y_i(1)]$ can provide abundant information for determining $z_s(i) - z_s(1)$ (see Fig. 10) assume that the slope of the weld pool surface along the y axis does not change from $(x_s(1), y_s(1), z_s(1))$ to $(x_s(i), y_s(i), z_s(i))$. This assumption will be reasonable if the height of the weld pool surface does not significantly

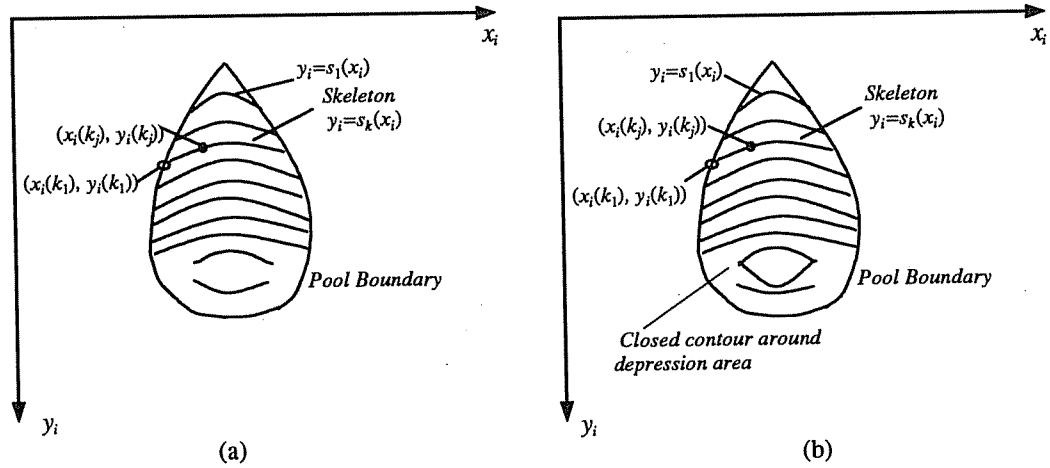

Fig. 9 Image features: (a) open-contour case, (b) closed-contour case

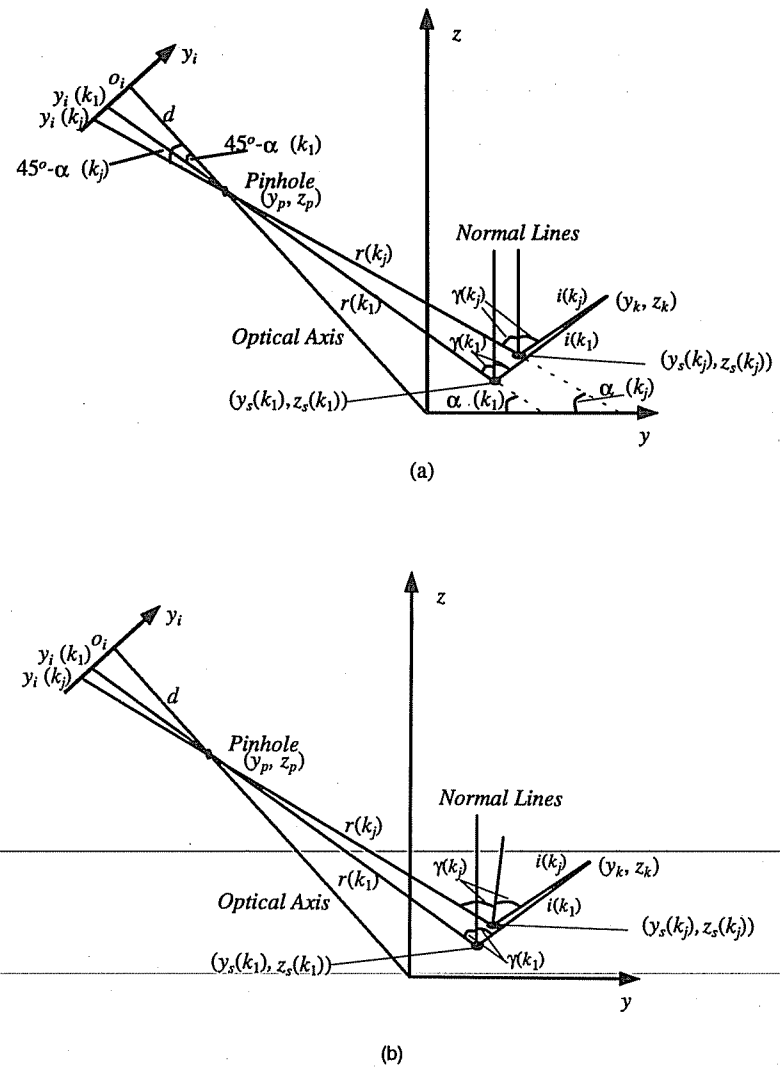

Fig. 10 Image coordinate difference and surface height variation: (a) zero surface slope and (b) non-zero and changing slope. $i(k_l)$ $(l = 1, j)$ = incident rays with slope $\rho_{iy}(k_l)$; $r(k_l)$ $(l = 1, j)$ = reflected rays with slope $-\rho_{ry}(k_l)$; $\gamma(k_l)$ $(l = 1, j)$ = incident and reflection angles, d = distance between the pinhole and o_i

vary longitudinally and $y_s(i) - y_s(1)$ is small. [It can be shown that both the height variation along the y direction and the maximum $y_s(i) - y_s(1)$ are indeed small.] In this case, for the sake of discussion convenience, the slope can first be assumd to be zero. Thus, the geometrical relationship of the parameters of interest can be illustrated in Fig. 10a. It can be shown that

$$-\frac{z_s(l) - z_p}{y_s(l) - y_p} = \frac{z_s(l) - z_k}{y_s(l) - y_k} = \rho_{iy}(l) \qquad (l = 1, i) \tag{8}$$

The following are generated:

$$\left.\begin{aligned} y_s(l) &= \frac{1}{2}\left(\frac{z_p - z_k}{\rho_{iy}(l)} + y_p + y_k\right) \\ z_s(k_l) &= \frac{1}{2}\left(\frac{y_p - y_k}{\rho_{iy}(l)} + z_p + z_k\right) \end{aligned}\right\} \qquad (l = 1, i) \tag{9}$$

Consequently,

$$z_s(i) - z_s(1) = \left(\frac{y_p - y_k}{2}\right)[\rho_{iy}(i) - \rho_{iy}(1)] \tag{10}$$

Also, from $\rho_{iy}(1) = tg\alpha(1)$ and the angular relationship shown in Fig. 10a, the following can be obtained:

$$tg[45° - \alpha(l)] = \frac{y_i(l)}{d} = \frac{1 - \rho_{iy}(l)}{1 + \rho_{iy}(l)} \qquad (l = 1, i) \tag{11}$$

where d is the distance from the pinhole to the image coordinate origin o_i. Thus, the following equation can be acquired:

$$\rho_{iy}(i) - \rho_{iy}(1) = \frac{2}{[1 + y_i(1)/d][1 + y_i(i)/d]}[y_i(1) - y_i(i)] \tag{12}$$

Also, d is much larger than the size of the imaging plane. Thus,

$$\begin{aligned} z_s(i) - z_s(1) &= -(y_k - y_p)[y_i(i) - y_i(1)] \\ &= -\gamma[y_i(i) - y_i(1)] \end{aligned} \tag{13}$$

where $y_k = (y_{k0} + y_{k1})/2$ is the y coordinate of the central line of the kth slit and $\gamma = (y_k - y_p)$ is a positive

constant for the addressed stripe. It can be seen that the height variation of the weld pool surface can be directly determined using the difference of their image coordinates.

When the slope is non-zero (see Fig. 10b), the following can be acquired:

$$y_s(i) = \frac{z_k - z_p + \rho_{ry}(i)y_p - \rho_{iy}(i)y_k}{\rho_{ry}(i) - \rho_{iy}(i)}$$
$$z_s(i) = \frac{\rho_{iy}(i)\rho_{ry}(i)(y_k - y_p) + \rho_{iy}(i)z_p - \rho_{ry}(i)z_k}{\rho_{iy}(i) - \rho_{ry}(i)} \quad (14)$$

Since the slope of the surface along the y axis can be assumed to be small, the accuracy of the approximation $\rho_{iy}(i) = -\rho_{ry}(i)$ will be sufficient to produce

$$z_s(i) = \frac{\rho_{ry}(i)(y_k - y_p) + z_p + z_k}{2} + \delta \quad (15)$$

where

$$\delta = \frac{y_k - y_p + z_p}{2}[\rho_{ry}(i) - \rho_{iy}(i)] \quad (16)$$

is determined by the surface slope. Thus,

$$z_s(i) - z_s(1) = -\left(\frac{y_p - y_k}{2}\right)[\rho_{ry}(i) - \rho_{ry}(1)] + \delta \quad (17)$$

It can be seen that in this case, the surface height variation is determined by both the image coordinate difference $[y_i(i) - y_i(1)]$ and the surface slope difference. However, when $[y_s(i) - y_s(1)]$ is small, the surface slope difference must be very small. The surface height variation is again determined primarily by the image coordinate difference $[y_i(i) - y_i(1)]$. As shown in Fig. 10b, $[y_s(i) - y_s(1)]$ can at most reach the level of the height difference. This is a very small figure for the pool length direction. Significant surface slope differences in this range cannot be expected in the non-impacted area in GTAW without filler. Thus, the image coordinate difference in an individual stripe can provide adequate information for estimating the surface height variation.

4.3 Adjacent stripes

It can also be shown that the distance of the image coordinate between two adjacent stripes can provide abundant information for the identification of the height difference. In this case, the incident rays come from different slits. Consider the kth and $(k + 1)$th slits. Denote $y_j = (y_{j0} + y_{j1})/2$ and $z_j = (z_{j0} + z_{j1})/2$ $(j = k, k + 1)$ [see equations (2)]. Thus, the projections of the kth and $(k + 1)$th slits on to the yz plane will be (y_k, z_k) and (y_{k+1}, z_{k+1}). The projections of the corresponding points on the weld pool surface are $(y_s(k), z_s(k))$ and $(y_s(k + 1), z_s(k + 1))$ (Fig. 11). It is known that the slit distance is small (1 mm) for the present sensor. Also, the height of the weld pool surface does not quickly change along its major axis. Thus, it can be assumed that the slope of the surface along the y axis does not change from $(y_s(k), z_s(k))$ and $(y_s(k + 1), z_s(k + 1))$ (Fig. 11). The following can be shown:

$$z_s(j) = \frac{z_p ctg\alpha(j) + z_j ctg\beta(j) + y_p - y_j}{ctg\alpha(j) + ctg\beta(j)} \quad (j = k, k + 1) \quad (18)$$

Assume that

$$\alpha(k + 1) = \alpha(k) - \Delta\alpha \quad (19)$$

It can be shown that

$$\beta(k + 1) = \beta(k) - \Delta\alpha \quad (20)$$

Thus,

$$z_s(k + 1) - z_s(k) = \frac{z_p ctg[\alpha(k) - \Delta\alpha] + z_{k+1} ctg[\beta(k) - \Delta\alpha] + y_p - y_{k+1}}{ctg[\alpha(k) - \Delta\alpha] + ctg[\beta(k) - \Delta\alpha]} - \frac{z_p ctg\alpha(k) + z_k ctg\beta(k) + y_p - y_k}{ctg\alpha(k) + ctg\beta(k)} \triangleq f(\Delta\alpha) \quad (21)$$

where f is a deterministic function for the given sensor configuration parameters and k, that is the height difference, is only determined by $\Delta\alpha$ (Fig. 11b). Furthermore, it can be shown that $\Delta\alpha$ is solely determined by the image coordinate difference. Thus, the image coordinate difference between different slits includes adequate information about the height variation of the weld pool surface in the non-impacted zone.

4.4 Impacted zone

Plasma jets can generate a significant impact on the weld pool. The weld pool is therefore depressed. Roughly speaking, the centre of the impacted zone has the lowest point on the weld pool surface. From this centre, the height of the weld pool surface increases along any direction. Thus, the slope of the weld pool surface changes its sign in the impacted zone. If the depression is significant, a laser stripe projected on to the impacted zone could develop into a closed-contour stripe. Thus, two modes of the reflected laser from the impacted zone are encountered, that is open contour or closed contour (Fig. 8).

As has been observed and analysed, the reflection at the impacted zone may no longer exhibit the pure stripe mode as it does in the non-impacted zone. In this case, the outline of the reflection as shown in Fig. 8 may be the only concern. This outline consists of the feature edges, that is two edges for the open-contour mode or three edges for the closed-contour mode. These feature edges are referred to as the upper edge, lower edge and second lower edge respectively (Fig. 8).

Extensive experimentation has shown that when the depression is shallow, the reflection at the impacted zone exhibits the open-contour mode. When the depression increases, the closed contour occurs. Also, the shape of the closed contour is directly determined by the depression. When the depression becomes significant, the maximum distance between the upper edge and the second lower edge of the closed contour increases. Hence, the distances between the upper edge and second lower edge to their adjacent stripes decrease when the symmetric axis of the weld pool is approached from the sides of the weld pool.

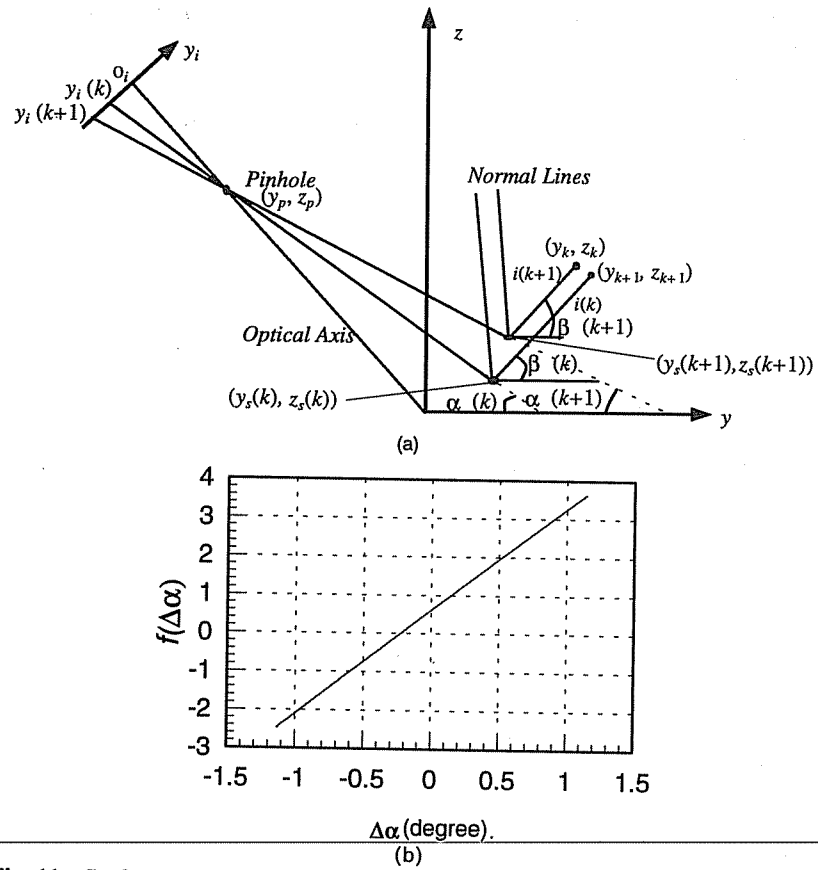

Fig. 11 Surface height difference between adjacent stripes: (a) geometrical relationship and (b) height variation with coordinate difference. The surface slope is assumed to be non-zero; $f(\Delta\alpha) = z_s(k+1) - z_s(k)$ is the height difference; $\Delta\alpha$ is the angular difference between the two reflected rays and is determined by the image coordinates; $z_p = 150$ mm, $y_p = -150$ mm; $y_k = 10$ mm, $z_k = 10$ mm; $y_{k+1} = 10 - 0.7$ mm, $z_{k+1} = 10 + 0.7$ mm; $\alpha(k) = 45° + 6.0°$; $\beta(k) = 45° - 6.0°$

The above observations on the reflection at the impacted zone can be sufficiently explained using the optical principle. Assume that the contour is produced by the kth slit. It is apparent that when the reflection surface is flat (Fig. 12a), among the rays dispersed from a point in the slit only one ray can cross the pinhole to be imaged on the imaging plane. Because of the continuity of the points in the slit, the sensed reflection is therefore a continuous region. In this case, only the open contour can be generated. When the closed contour occurs, the image of the slit is segmented into two continuous regions. These two regions are produced by two regions of the slit. The region boundary point of the slit produces image points P_1 and P_2 (Fig. 12b). Because $\beta_1 > \beta_2$ and $\gamma_1 < \gamma_2$, θ_1 must be larger than θ_2. Thus, the slopes of the corresponding surface points must be different. Also, it can be seen that the slope difference is directly determined by the difference between P_1 and P_2. If the difference between P_1 and P_2 is large, the slope difference must also be large. In order to produce a large slope difference, a deep depression is required. Roughly speaking, the difference between P_1

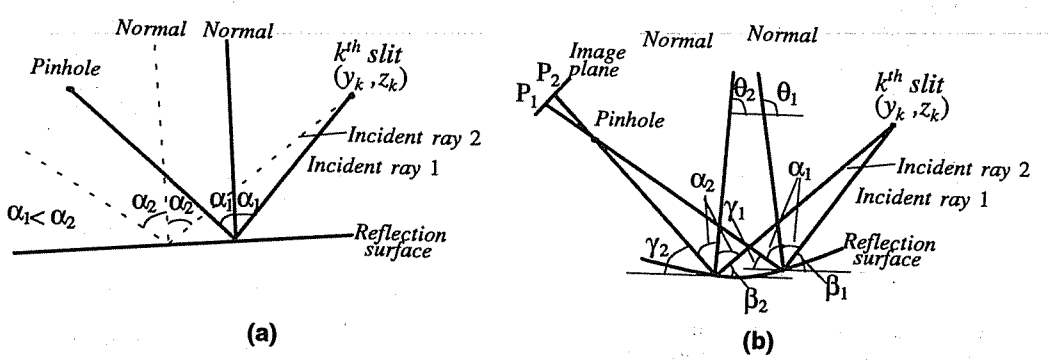

Fig. 12 Closed-contour development: (a) flat surface, (b) non-flat surface

and P_2 reflects the depression. Thus, when the symmetric axis of the impacted area, which is a line parallel with the y axis, is approached from the sides of the weld pool, the difference between P_1 and P_2 increases (Fig. 4b and c). If the depression is not significant enough, the difference between P_1 and P_2 will be too small to distinguish. In this case, no closed contour will be observed.

4.5 Image features

It can be seen that the surface information is contained in the stripes. The stripes in the non-impacted zone can be represented by their skeleton (Fig. 9). The stripes at the impacted zone can be characterized by the upper and lower edges as defined in Fig. 8. The skeleton of the stripes in the non-impacted zone and outline edges at the impacted zone are referred to as the skeleton of the specular reflection. Thus, the skeleton of the specular reflection and pool boundary are selected as the image features.

5 POOL SURFACE CALCULATION

A real-time image processing technology has been developed to extract the image features in 250 ms from the acquired image (**41**). [An example is shown in Fig. 13b, and more can be seen in reference (**41**).] Another algorithm must be developed to calculate the weld pool surface from the processed image.

The procedure that determines the image from a given weld pool surface is called the forward problem. The implementation of the forward calculation needs more than 5 seconds on a PC-486DX66. The extraction of the pool surface shape from the image features is a much more difficult task. In fact, for any bright point on the acquired image, a line can be made to connect this point to the pinhole. This line is the reflected ray and may be reflected from numerous spatial points, depending on the surface slope (normal), which is also unknown. The determination of the weld pool surface from the acquired image is referred to as the inverse problem.

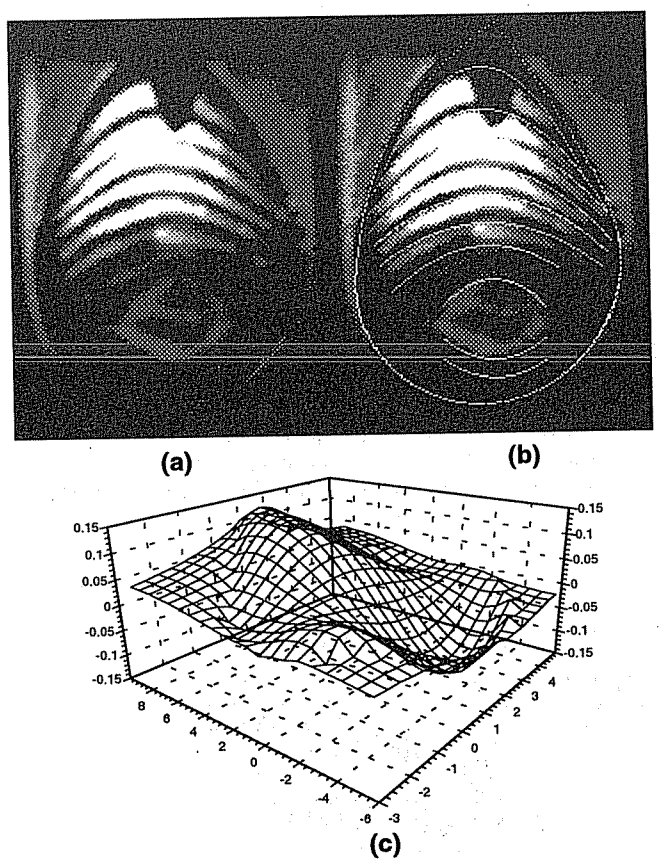

Fig. 13 An example of sensing of weld pool surface: (a) acquired original image, (b) processed image, (c) resultant surface of weld pool

A possible straightforward way to solve the inverse problem is the optimization, that is finding a surface equation $z = f^*(x, y)$ that minimizes the cost function:

$$J = \|M_{\text{acquired}} - M_f\|$$

where M_{acquired} is the binary matrix of the acquired image, M_f is the binary matrix of the calculated image using f and $\|\cdot\|$ represents the norm of the matrix. In the present case, the second-order norm can be used. To obtain the binary matrix for the acquired image, preprocessing of the image is required to detect the pool boundary and then determine the imaging points of the reflected structured light within the weld pool boundary. The imaging points of the structured light reflection from the weld pool surface will be denoted as one and the remaining area on the image will be denoted as zero. For the calculated image, the binary matrix can be directly acquired from the forward calculation procedure.

It can be seen that numerous calculations of the forward problem will be required in order to find the optimal candidate surface for the weld pool surface. As has been stated, implementing the forward calculation on a PC-486DX66 in C requires more than 5 seconds. It seems impossible to determine the weld pool surface by the above optimization procedure.

The difficulty in calculating the surface from the image features is caused by the coupling between the surface height and slope. To solve this problem, an iterative algorithm can be used. Firstly, a flat surface can be assumed. Based on this assumed surface, the slope corresponding to each stripe point on the image can be calculated using the reflection law. The calculated slopes can be further used to fit a surface if an additional boundary condition is available. If the estimated slopes are more accurate than zero, the fitted surface will be a more accurate estimate of the weld pool surface than the flat surface. Using the heights associated with the fitted surface, the slopes can be calculated again based on the reflection law. The new estimate of the surface can therefore be acquired. Thus, a surface series can be acquired. If the surface series converges, the resultant surface will be an accurate estimate of the weld pool surface. It has been assumed that the slopes calculated using the initial flat surface are more accurate than the zero slopes associated with the initial flat surface. Thus, the new surface will be a more accurate estimate of the weld pool surface than the flat surface. Using this more accurate surface, the slopes can be calculated more accurately than by using the flat surface. Hence, the surface estimate will converge to the actual weld pool surface and an accurate weld pool surface can be acquired.

An algorithm has been developed to implement the above iterative calculation for the weld pool surface. An

example is shown Fig. 13. However, 1 second is required for the current algorithm. This speed is not sufficient for the real-time implementation. Currently, the algorithm is being optimized and implemented on an advanced image processing system. It is expected that the weld pool surface will be calculated at 5 Hz which could be recognized as real-time in most applications.

6 CONCLUSIONS

The proposed system can sense the deformation of the weld pool despite the strong arc and mirror-like pool surface. The sensing principle can be exactly described using the mathematical model derived from the reflection law. Utilizing the mathematical model, the image corresponding to an assumed surface can be determined based on the surface model and sensor parameters. The deformation of the stripes reflect the deformation of the weld pool surface. Especially, the contour modes, open contour or closed contour, are directly determined by the degree of the depression, and therefore by the plasma impact. Although the sensing principle is clear, no explicit models exist for directly calculating the weld pool surface from the image features. To solve this inverse problem, an iterative algorithm has been proposed. However, the calculation speed is reduced. Currently, 1 second is needed to obtain the weld pool surface from the acquired image. An investigation is being done to promote the speed to 5 Hz in order to apply this technique in real-time sensing and control.

This work has been restricted to GTA welding. For GMA welding, the weld pool surface is subjected to periodic impacts from droplets. The surface oscillation is substantial. In order to trace the GMA weld pool surface, the imaging and processing speeds have to be significantly increased. Higher speeds will also be required if a dynamic, rippling GTA weld pool needs to be traced.

ACKNOWLEDGEMENT

This work was supported by the National Science Foundation under contract DMI-9414530.

REFERENCES

1 **Rokhlin, S. I.** and **Guu, A. C.** A study of arc force, pool depression, and weld penetration during gas tungsten arc welding. *Weld. J.*, 1993, **72**(8), 381s–390s.

2 **Lin, M. L.** and **Eagar, T. W.** Influence of surface depression and convection on arc weld pool geometry. In *Transport phenomena in material processing* (Eds M. M. Chen, J. Mazumder and C. L. Tucker III), 13–18 November 1983, ASME PED-10, pp. 63–69 (American Society of Mechanical Engineers, New York).

3 **Lin, M. L.** and **Eagar, T. W.** Influence of arc pressure on weld pool geometry. *Weld. J.*, 1985, **64**(6), 163s–169s.

4 **Zhang, Y. M., Cao, Z. N.** and **Kovacevic, R.** Numerical analysis of fully penetrated weld pools in gas tungsten arc welding. *Proc. Instn Mech. Engrs, Part C*, 1996, **210**(C2), 187–195.

5 **Tsai, M. C.** and **Kou, S.** Electromagnetic-force-induced convection in weld pools with a free surface. *Weld. J.*, 1990, **69**(6), 241s–246s.

6 **Choo, R. T. C., Szekely, J.** and **Westhoff, R. C.** Modeling of high-current arcs with emphasis on free surface phenomena in the weld pool. *Weld. J.*, 1990, **69**(9), 346s–361s.

7 **Kim, J.-W.** and **Na, S.-J.** A study on the three-dimensional analysis of heat and fluid flow in gas metal arc welding using boundary-fitted coordinates. In *Welding and joining processes* (Eds E. Kannatey-Asibu Jr, H. S. Cho and S. Fukuda), 1–6 December 1991, ASME PED-51, pp. 159–173 (American Society of Mechanical Engineers, New York).

8 **Kim, J.-W.** and **Na, S.-J.** Effect of weld pool deformation on weld penetration in stationary gas tungsten arc welding. *Weld. J.*, 1992, **71**(5), 179s–192s.

9 **Renwick, R. J.** and **Richardson, R. W.** Experimental investigation of GTA weld pool oscillations. *Weld. J.*, 1983, **62**(2), 29s–35s.

10 **Zacksenhouse, M.** and **Hardt, D. E.** Weld pool impedance identification for size measurement and control. *Trans. ASME, J. Dynamic Systems, Measmt and Control*, 1983, **105**(3), 179–184.

11 **Tam, A. S.** and **Hardt, D. E.** Weld pool impedance for pool geometry measurement: stationary and nonstationary pools. *Trans. ASME, J. Dynamic Systems, Measmt and Control*, 1989, **111**(4), 545–553.

12 **Xiao, Y. H.** and **Ouden, G. den** A study of GTA weld pool oscillation. *Weld. J.*, 1990, **69**(8), 298s–293s.

13 **Sorensen, C. D.** and **Eagar, C. D.** Measurement of oscillations in partially penetrated weld pools through spectral analysis. *Trans. ASME, J. Dynamic Systems, Measmt and Control*, 1998, **112**(3), 463–468.

14 **Yoo, C. D.** Effects of weld pool conditions on pool oscillation. PhD dissertation, The Ohio State University, 1990.

15 **Xiao, Y. H.** and **Ouden, G. den** Weld pool oscillation during GTA welding of mild steel. *Weld. J.*, 1993, **72**(8), 428s–434s.

16 **Nagarajan, S., Banerjee, P., Chen, W. H.** and **Chin, B. A.** Control of the welding process using infrared sensors. *IEEE Trans. Robotics and Automn*, 1992, **8**(1), 86–93.

17 **Nagarajan, S., Chen, W. H.** and **Chin, B. A.** Infrared sensing for adaptive arc control. *Weld. J.*, 1989, **68**(11), 462s–466s.

18 **Chen, W. H.** and **Chin, B. A.** Monitoring joint penetration using infrared sensing techniques. *Weld. J.*, 1990, **69**(4), 181s–185s.

19 **Banerjee, P.** and **Chin, B. A.** Front-side-sensor-based dynamic weld penetration control. 1993 AWS Convention, Houston, Texas, 25–29 April 1993, Abstracts of papers, pp. 10–11 (AWS).

20 **Beardsley, H. E., Zhang, Y. M.** and **Kovacevic, R.** Infrared sensing of full penetration state in gas tungsten arc welding. *Int. J. Mach. Tool and Mfg*, 1994, **34**(8), 1079–1090.

21 **Hardt, D. E.** and **Katz, J. M.** Ultrasonic measurement of weld penetration. *Weld. J.*, 1984, **63**(9), 273s–281s.

22 **Lott, L. A.** Ultrasonic detection of molten/solid interfaces in weld pools. *Mater. Evaluation*, 1983, **42**, 337–341

23 **Lott, L. A., Johnson, J. A.** and **Smartt, H. B.** Real-time ultrasonic sensing of arc welding process. Proceedings of 1983 Symposium on *Nondestructive evaluation applications and materials processing*, Metals Park, Ohio, 1984, pp. 13–22 (ASM International).

24 **Johnson, J. A., Carlson, N. M.** and **Lott, L. A.** Ultrasonic wave propagation in temperature gradients. *J. Nondestructive Evaluation*, 1988, **6**(3), 147–157.

25 **Carlson, N. M.** and **Johnson, J. A.** Ultrasonic sensing of weld pool penetration. *Weld. J.*, 1988, **67**(11), 239s–246s.

26 **Rokhlin, S. I., Cho, K.** and **Guu, A. C.** Closed-loop process control of weld penetration using real-time radiography. *Mater. Evaluation*, 1989, **47**, 363–369.

27 **Guu, A. C.** and **Rokhlin, S. I.** Computerized radiographic weld penetration control with feedback on weld pool depression. *Mater. Evaluation*, 1989, **47**, 1204–1210.

28 **Cannon, I., Maram, J.** and **Smith, M.** Weld penetration sensor for an experimental welder. *Trans. NAMRC/SME*, 1987, **XV**.

29 **Zhang, Y. M.**, *et al.* Determining joint penetration in GTAW with vision sensing of weld face geometry. *Weld. J.*, 1993, **72**(10), 463s–469s.

30 **Zhang, Y. M., Kovacevic, R.** and **Wu, L.** Closed-loop control of weld penetration using front-face vision sensing, *Proc. Instn Mech. Engrs, Part I*, 1993, **207**(I1), 27–34.

31 **Zhang, Y. M., Kovacevic, R.** and **Wu, L.** Dynamic analysis and identification of gas tungsten arc welding process for weld penetration control. *Trans. ASME, J. Engng for Industry*, 1996, **118**(1), 123–136.

32 **Kovacevic, R.** and **Zhang, Y. M.** Apparatus and method for measuring 3-D weld pool shape. US Pat. 5,481,085, 2 January 1996.

33 **Kovacevic, R., Zhang, Y. M.** and **Ruan, S.** Sensing and control of weld pool geometry for automated GTA welding, *Trans. ASME, J. Engng for Industry*, 1995, **117**(2), 210–223.

34 **Cook, G. E.** Robotics arc welding: research in sensory feedback control, *IEEE Trans. Ind. Electronics*, 1983, **IE-30**(3).

35 **Zhang, Y. M., Kovacevic, R.** and **Wu, L.** Sensitivity of front-face weld geometry in representing the full penetration, *Proc. Instn Mech. Engrs, Part B*, 1992, **206**(B3), 191–197.

36 **Agapakis, J. E.**, *et al.* Joint tracking and adaptive robotic welding using vision sensing of weld joint geometry. *Weld. J.*, 1986, **65**(11), 33–41.

37 Klein, M. V. and **Furtak, T. E.** *Optics*, 1986, Ch. 3 (John Wiley, New York).

38 Kovacevic, R. and **Zhang, Y. M.** Machine vision recognition of weld pool in gas tungsten arc welding. *Proc. Instn Mech. Engrs, Part B*, 1995, **209**(B2), 141–152.

39 Hoffman, T. Real-time imaging for process control. *Advanced Mater. and Processes*, 1991, **140**(3), 37–43.

40 Dawson-Howe, K. M. and **Vernon, D.** Simple pinhole camera calibration. *Int. J. Imaging Systems and Technol.*, 1994, **5**, 1–6.

41 Kovacevic, R. and **Zhang, Y. M.** Real-time image processing for monitoring of free weld pool surface. *Trans. ASME, J. Engng for Industry*, November 1996, **118**(4).